Applications of Poincaré Search Maps for Space-Based Cislunar SDA Detection

Raymond H. Wright[a], **Naomi Owens-Fahrner**[a], **Luke Tafur**[a], **and Joshua Wysack**[a]
[a]*BAE Space Mission Systems, 7 Longs Peak Drive, Broomfield, USA*

ABSTRACT

Cislunar space, the region governed by the gravitational forces of both the Earth and the Moon, is rapidly becoming a focal point for international, governmental, scientific, and commercial ventures, drawn by its abundant resources and strategic importance [1]. The increasing activity in this region is transforming it into a crowded and complex environment, presenting significant challenges for Space Domain Awareness (SDA) and Space Traffic Management (STM). Current methods, which are primarily designed for monitoring Resident Space Objects (RSOs) within Earth's Geostationary Orbit (GEO), are ill-equipped to manage the vast and dynamic cislunar volume.

Addressing these challenges requires innovative solutions that can adapt to the unique conditions of cislunar space. Poincaré Search Maps (PSMs) offer a groundbreaking approach by leveraging mission-based orbital dynamics to optimize surveillance efforts. PSMs strategically position virtual surfaces in space, focusing on high-traffic areas such as Lagrange points, where orbits converge in a predictable manner. These points are of particular interest because they serve as natural gravitational hubs, making them critical for monitoring the movement of RSOs in cislunar space. By concentrating surveillance on these key areas, PSMs enable more efficient and effective tracking of objects, significantly improving SDA capabilities in this expansive region.

The adoption of PSMs represents a transformative shift in how SDA is conducted in cislunar space, moving from a reactive to a proactive approach. Instead of merely responding to detected threats or anomalies, this strategy allows for the anticipation and prevention of potential collisions and other hazards. As cislunar space becomes increasingly populated with diverse activities, the ability to maintain safety and security in this region is paramount. The application of PSMs provides a robust framework for achieving these goals, offering a scalable and adaptable solution that can evolve alongside the growing demands of cislunar operations. This proactive approach to SDA not only safeguards ongoing missions but also lays the groundwork for the sustainable development of cislunar space, ensuring that this critical region remains accessible and secure for future generations.

1. INTRODUCTION

The expansion of commercial and scientific activities beyond the geostationary sphere necessitates advancements in Space Situational Awareness (SSA) and SDA search capabilities. Wysack [2] explored various architectures aimed at monitoring volumes as expansive as ten times that of a GEO orbit (10xGEO). While this region remains largely speculative in terms of practical applications, it signifies a potential frontier for future space activities and exploration beyond traditional Earth orbits. In contrast, the region known as cislunar space is less speculative and more active. Cislunar space encompasses the area where Resident Space Objects (RSOs) orbit the earth and Moon, and the trajectories that traverse between the two. Hozlinger defines cislunar space as "*the volume of space influenced by the Earth and/or Moon*" [3].

Figure 1 is a two-dimensional illustration, not to scale, of the difference between a 10xGEO and cislunar volume, with the caveat that there is no official definition of cislunar space. Clearly the enormity of 10xGEO and cislunar volumes present challenges to current ground and space-based detection activities.

Previous work [4] explored the concept of leveraging natural bottlenecks that exist within the Earth-Moon (EM) Circular Restricted 3-Body Problem (CR3BP) to reduce the search space for SDA and STM missions. By focusing on these bottlenecks, a monitoring plane was found to efficiently cover key trajectories, potentially detecting over 80% of traffic with a limited number of observers. This approach provides the foundation to simplify SDA and STM monitoring and tracking demands in a full cislunar volume. This paper will build upon this idea of optimizing surveillance architectures by applying PSMs strategically within the cislunar volume. By focusing on scientific and commercial strategic locations such as EM Lagrange points and increasing detection sensitivity by using space-based infrared sensors, this approach enhances detection capabilities while reducing searching resources. This evolution from reactive to proactive SDA aims to improve safety and security in the increasingly active cislunar space.

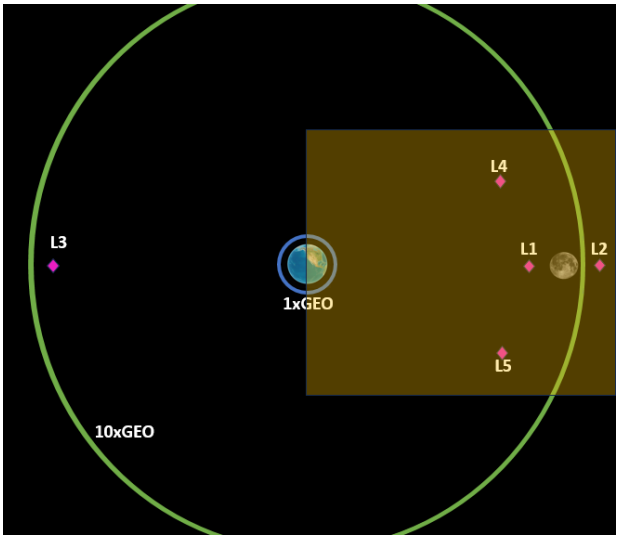

Fig. 1: A two dimensional layout of the Earth-Moon system with a 10xGEO circle and the approximate cislunar definition.

1.1 Background

Prior to addressing the complexities of NxGEO or cislunar search, it is essential to summarize the challenges associated with monitoring all objects within a 1xGEO volume. Bloom [5] investigated various existing and future architectures needed to reduce detection outages and increase observability out to 1xGEO. Current ground-based systems are limited to useful geographical locations. Space-based systems are considered more expensive to build and replenish. Bloom also found that there are regions of the 1xGEO sphere that have a persistent detection gap from ground systems and greater than a 7-hour gap for space-based systems. Bloom proposed a combination of future ground and space-based architectures that could reduce the gap to less than 2 hours, but still not eliminate gaps.

Expanding from everything within a 1xGEO sphere, to SDA/STM missions focused on 1xGEO to 10xGEO, Wysack [2] explored architectural designs that would support early Indications and Warnings (I&W). For a search mission architecture to achieve over a 90% capacity coverage, over 70 new space-based systems are needed in various orbital regimes such as Resonant Planar Orbits, and L_3, L_4, and L_5 periodic orbits.

1.2 Definition of Poincaré Search Maps

Attempting to reduce the number of vehicles required and cost in architecture designs, the PSMs provide a method to search a volume more efficiently by reducing the search volume. Mathematically, a surface is a generalization of a plane that may exhibit curvature and enclose a volume, forming a bounded surface. A PSM is defined as a location in space, whether a plane or a surface, where one or more transiting bodies, such as satellites or asteroids, intersect with specified entry and exit points. If the PSM is defined as a plane, the entry and exit points may coincide.

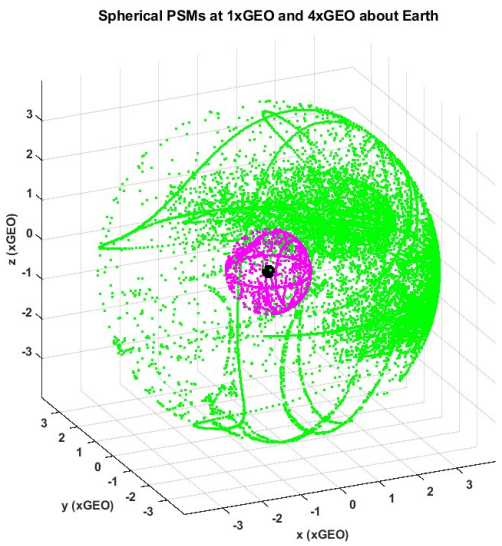

(a) Two spherical PSMs placed about Earth

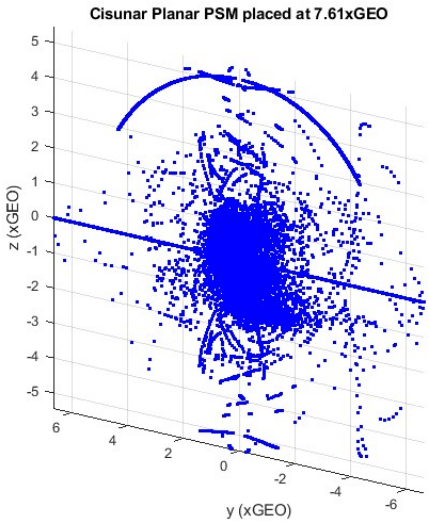

(b) A Planar PSM placed in cislunar space between the Earth and Earth-Moon L_1

Fig. 2: Example PSMs of various shapes and locations in the Earth-Moon system

Every dot in Figure 2 represents a trajectory that crossed a PSM surface. For Figure 2a, the two colors represent specific xGEO crossings, where pink is 1xGEO crossing and green is a 4xGEO crossing. The shape of the PSMs are spherical shells and centered about Earth (black center). Whereas the shape of the PSM in Figure 2b mirrors a traditional rectangular plane with the trajectory crossings mapped in either blue. The planer PSM is placed at 7.61xGEO radii from Earth.

A common unit of measure used to discuss distance is the standard SI unit the kilometer (km). Table 1 highlights how much larger a 4xGEO or 10xGEO is when compared to a 1xGEO volume. It also demonstrates the need to move away from the km and instead, discuss the vastness of space in terms of xGEO radii, where 1xGEO is a radius of 42,164km and the origin is centered at Earth. This places the average position of the Moon at approximately 9.25xGEO (384,000km) away from the Earth as shown in Figure 3. This figure is not to scale and is used to illustrate the xGEO dimensionality. Volume can be calculated in a ratio of xGEO as show in Table 1. Using the standard equation for a cylinder, $V = \pi r^2 h$, an example cislunar volume can be calculated where r is the distance from the Earth-Moon axis to either L_4 or L_5, and h is the distance from Earth to L_2. It is clear that the cislunar volume is much larger than 1xGEO, it consumes a significant portion of the 10xGEO volume, and it is contextually easier to discuss in terms of xGEO.

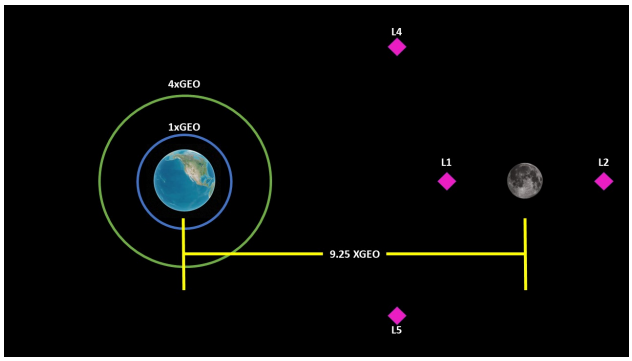

Fig. 3: Defining cislunar space. Lagrange Point 3 is not shown in the figure (it would be to the left of the Earth).

Table 1: Comparing the vastness of 10xGEO and Cislunar Volume

NxGEO	Volume (km^3)	Volume Increase over 1xGEO
1	$3.14x10^{14}$	-
4	$2.01x10^{16}$	$\sim$ 64X
Example Cislunar	$2.25x10^{17}$	$\sim$ 719X
10	$3.14x10^{17}$	$\sim$ 1000X

2. APPROACH

To refine the scope of mission planning and execution, recent missions utilized a subset of trajectories which serve as a foundation for defining the trajectory shapes and optimal placements of. By analyzing these trajectories, one can more accurately determine the most efficient paths for spacecraft, ensuring that the placement and configuration of PSMs are tailored to meet the specific needs of each mission.

2.1 Trajectories in Cislunar Space

As stated earlier, PSMs are mission dependent and can be placed anywhere in space. Using the volume Example Cislunar volume defined in Table 1 and Figure 2, the defined mission has two goals:

- Detect trajectories that transit in cislunar space between the Earth and Moon
- Monitor RSOs that are in periodic orbits about L_1, the Moon, and L_2

The first goal investigates transit through the cislunar corridor using PSMs. Two types of traversals are investigated, direct transfers and invariant manifolds. Direct transfers are the most common transit method which require a significant amount of fuel mass to provide sufficient ΔV. The second method are invariant manifolds [4] which require no ΔV once entered, to reach either the Earth or Moon.

The second goal of the mission focuses on monitoring periodic orbits in the vicinity of the lunar region with PSMs. This involves tracking and analyzing orbits that exhibit regular, repeating patterns around the Moon and/or Lagrange points, contributing to a comprehensive understanding of the dynamical environment within the cislunar space.

2.1.1 Direct Transfer Orbits

A direct transfer orbit is a trajectory between the starting and end point without additional orbital maneuvers. This approach contrasts with more complex trajectories that might involve multiple orbits and/or gravity assists. One of the most common direct transfers used today is a Hohmann Transfer [6] because of the simplicity of the design, minimal $\Delta V s$ and short transit times [7]. Another transfer is the Ballistic Capture [8] method which has been successfully used by NASA and its CAPSTONE mission, and JAXA for the SLIM mission.

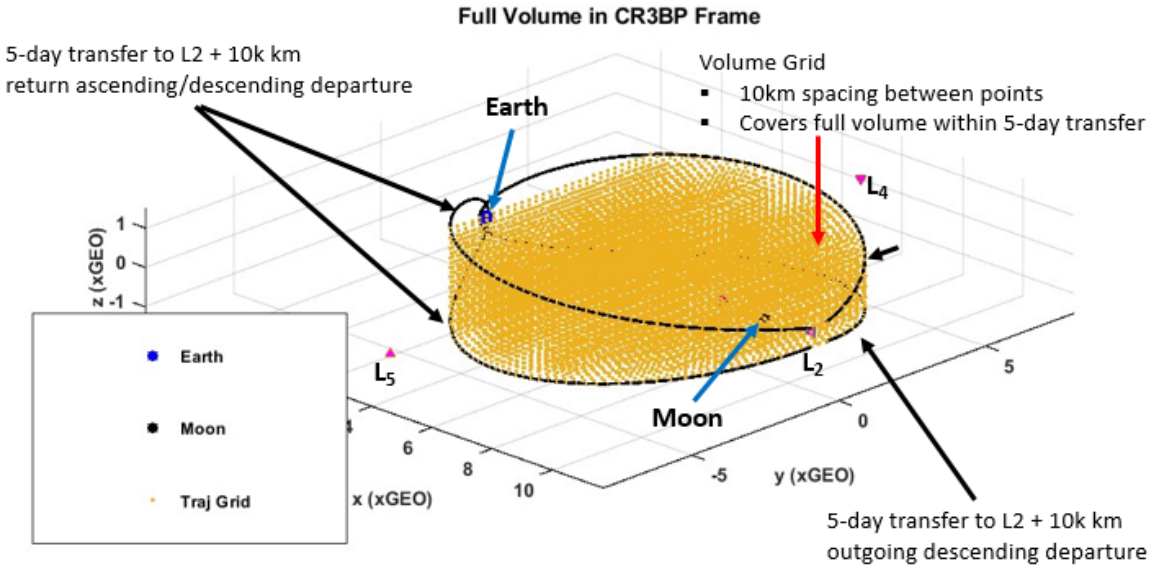

Fig. 4: A volume depicted by a grid of points as a result of the parametric study. The grid depicts possible Hohmann and faster trajectories between the Earth and Moon capped at a five-day time of flight.

Figure 4 illustrates the outcomes from a parametric study comparing Hohmann transfers with faster transfers between Earth and the Earth-Moon L_2 point. In this study, the maximum allowable Time Of Flight (TOF) is set to five days. The parameters under investigation include the injection velocity, Relative Right Ascension, and the True Anomaly at which the ΔV is applied. The trajectories are terminated at a final position 10,000 km beyond Earth-Moon L_2, extending to the periphery of cislunar space. The black lines in the figure represent the boundary trajectories, which correspond to the longest TOF. The grid of points shown in the figure is spaced 10,000 km apart and delineates the volume of space that a spacecraft could traverse via a direct transfer within the five-day constraint. Notably, the volume available for traversal decreases as the distance from Earth increases. Instead of searching the entire volume of grid points, a PSM can be strategically placed to reduce the volume while still capturing the paths of interest. In Figure 5, a rectangular PSM is placed at 7.97 to 8.155 xGEO along the Earth-Moon axis. This position along the axis resides between the Earth and L_1.

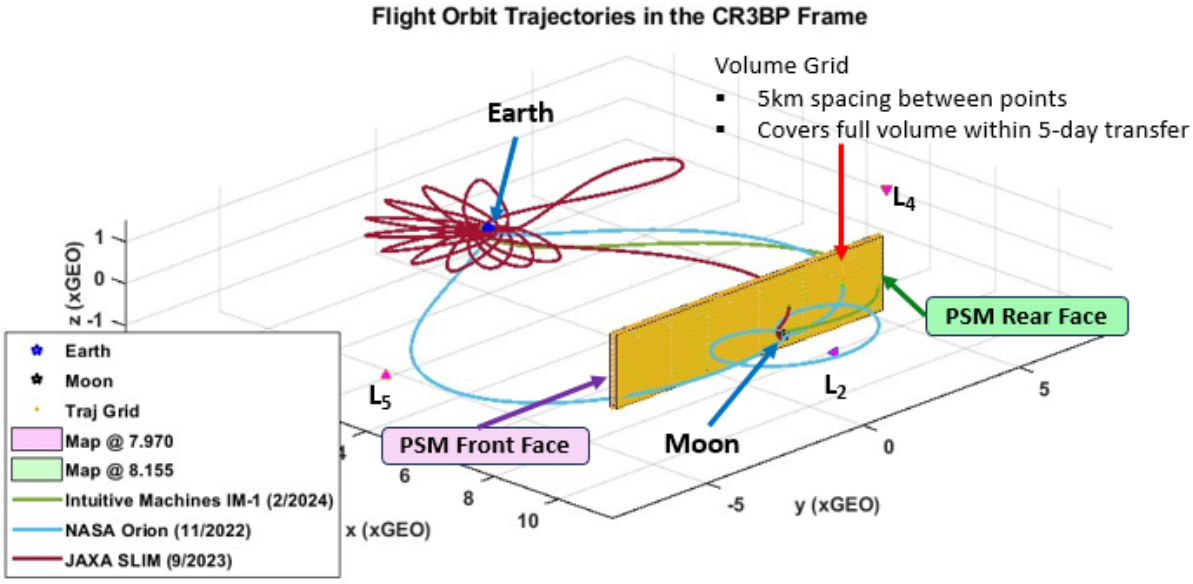

Fig. 5: A PSM placed at 7.97 to 8.15xGEO capturing a portion of the direct transfer orbit grid.

Placing the PSM, in Figure 5, near L_1 reduces the extents of the PSM in the Y and Z directions, while still capturing all potential trajectories from the parametric study. A mission designed around this PSM can be designed around a cislunar volume that is equivalent to 1.81 times that of 1xGEO volume, see Table 2. Three recent mission trajectories are also displayed in the figure, NASA's Orion, Intuitive Machines IM-1, and JAXA's SLIM trajectories were converted from JPL's Horizon [9] inertial frame to the CR3BP. All three missions cross the defined PSM.

Table 2: PSM bounds and volume for direct transfer trajectories

PSM #	X-Bounds (xGEO)	Y-Bounds (xGEO)	Z-Bounds (xGEO)	Volume Increase over 1xGEO
1	[7.97, 8.15]	[-4.26, 4.26]	[-0.88, 0.88]	0.65

2.1.2 Low-Energy Manifolds

An invariant manifold, or simply manifold, is an orbital trajectory that remains constant and time-invariant for a given set of initial conditions [4]. Once an RSO enters a manifold, it requires no additional ΔV to maintain its course to the final destination. These trajectories are of great interest in the science and commercial industries because of the potential savings in fuel mass.

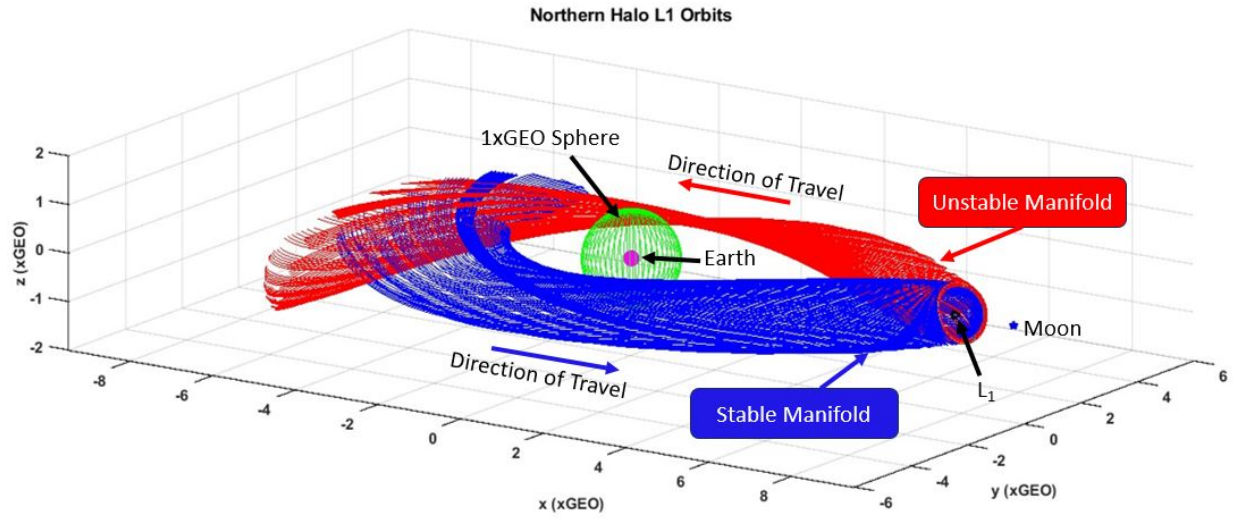

Fig. 6: Manifolds entering and exiting Earth-Moon L_1 for a sample of Northern Halo Orbits. The figure is correctly scaled.

Depicted in Figure 6 is a set of manifolds related to the Northern Halo family of orbits that orbit about L_1. There are two distinct "tube-like" shapes that have a common starting location. These tubes are the manifolds. One manifold contains trajectories heading towards L_1, while the other departs L_1. The magenta sphere at the origin (0, 0, 0) represents Earth to actual scale. The green sphere is the 1xGEO sphere and the axes are defined in terms of xGEO radii from Earth.

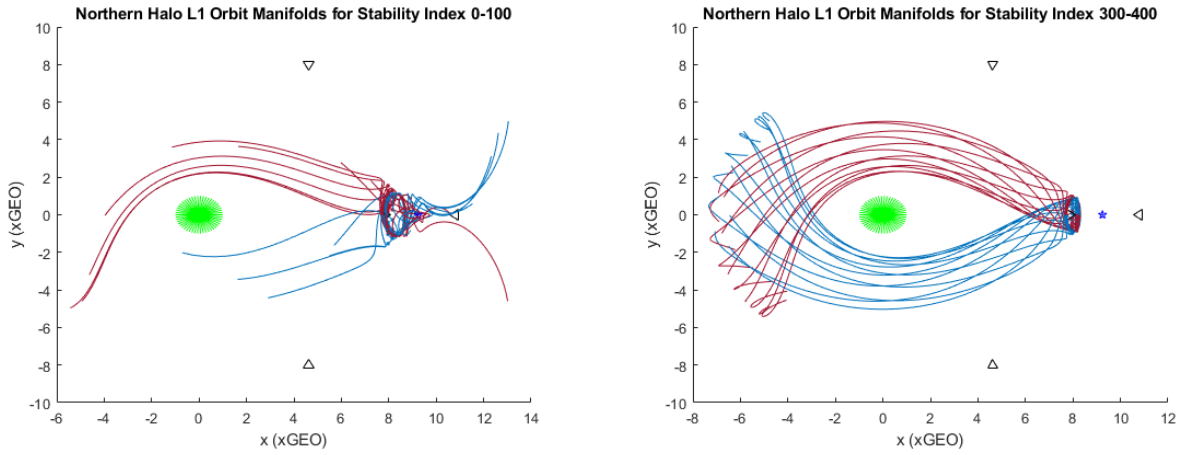

(a) Stability Indices 0 - 100

(b) Stability Indices 300 - 400

Fig. 7: Northern Halo Orbit Manifolds about L_1

Not all manifolds exhibit the same degree of definition as those depicted in Figure 6. In Figures 7a and 7b, blue represents orbits approaching L1, while red indicates orbits moving away from it. Unlike Figure 7b where manifolds are clearly defined, Figure 7a shows less defined manifolds where, for instance, an RSO could potentially orbit the Moon, pass by L2, and exit the Earth-Moon system, depending on its initial conditions. The variation in manifold shapes is associated with the stability index: a lower stability index signifies a more stable periodic orbit from which the manifold is derived, whereas a higher stability index suggests that less energy is required for the RSO to exit the periodic orbit, resulting in more distinctly structured manifolds. To obtain manifolds with a well-defined tube shape, it is generally found that the stability index should exceed approximately 100, though this threshold can vary among different families. Table 3 provides a summary of periodic orbit families and their corresponding stability indices,

with bold and italicized values indicating those used for generating the PSM crossings based on visual inspection of the manifolds.

Table 3: Number of CR3BP Orbit Families from JPL database [10] within Stability Index Range

Family Name	Stability Index				
	0-100	100-200	200-300	300-400	400+
Lyapunov about L_1	554	148	***42***	***27***	***266***
Lyapunov about L_2	735	94	***45***	***34***	***168***
Northern Halo about L_1	394	152	307	***223***	***71***
Northern Halo about L_2	1041	***110***	***82***	***74***	***228***
Southern Halo about L_1	394	152	307	***223***	***71***
Northern Vertical about L_1	544	545	***24***	0	0
Northern Vertical about L_2	570	***26***	***239***	0	0
Axial about L_1	0	0	***1250***	0	0

Using this approach, twelve equidistant initial conditions were selected around each periodic orbit that satisfied the stability index criteria. Each initial condition was then propagated to produce twelve manifold trajectories per periodic orbit. The DRO and Southern Dragonfly orbits were ignored due to the inability to generate well-formed manifold tubes. Based on initial findings, the PSM #1 in Table 2 was chosen because it captures a majority of the manifold crossings and is still between the Earth and the Moon. This PSM reduces the search volume while capturing a majority of the trajectories that can be monitored by choosing a location where the trajectories converge down to a smaller area. PSM #1 can be seen in Figure 8b along with the Northern Vertical orbits about L_1 in Figure 8a. For ease of visibility, only the front (magenta plane at 7.97xGEO radii) and rear (yellow plane at 8.15xGEO radii) surfaces are shown in Figure 8b with a point cloud of manifold crossings.

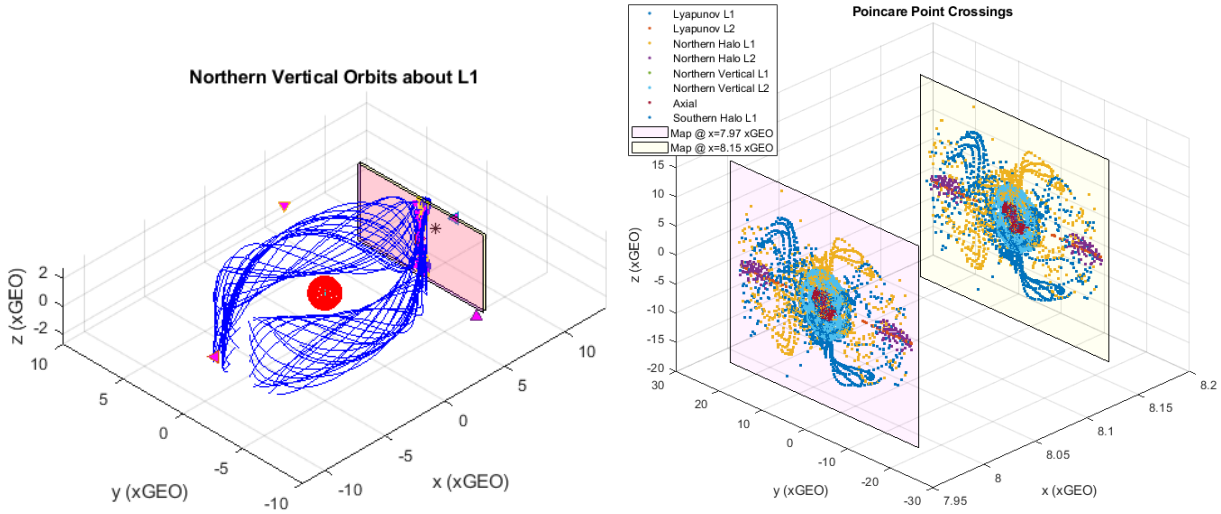

(a) Northern Vertical Manifolds about L_1

(b) PSMs at x = 7.97 and 8.15 xGEO for all families

Fig. 8: Poincaré Surface Maps and Invariant Manifolds

Analysis of the families, as presented in Table 4, reveals that the large bounds are predominantly due to the Halo orbits, which contribute significantly to the size increase. Additionally, some Lyapunov orbits that exit the L_2 gateway and return across the plane also contribute to this effect. The bounds are defined such that all of the trajectories intersecting the plane are captured.

It should be noted that the volume increase does not show the full story, since for Lyapunov orbits the volume increase is 0, but the y-bounds of the full search volume are increased. These manifolds can be seen visually in Figure 9a for the Lyapunov orbits and in Figure 9b for the Halo orbits.

Table 4: PSM Bounds by Family for the Invariant Manifolds

Family	X-Bounds (xGEO)	Y-Bounds (xGEO)	Z-Bounds (xGEO)	Volume Increase over 1xGEO
Lyapunov about L_1	[7.97, 8.15]	[-3.24, 2.83]	[0, 0]	0
Lyapunov about L_2	[7.97, 8.15]	[-20.26, 19.34]	[0, 0]	0
Northern Halo about L_1	[7.97, 8.15]	[-18.86, 19.91]	[-11.58, 16.12]	46.31
Northern Halo about L_2	[7.97, 8.15]	[-20.44, 19.65]	[-2.35, 1.94]	7.42
Southern Halo about L_1	[7.97, 8.15]	[-19.75, 20.45]	[-15.31, 11.58]	46.61
Northern Vertical about L_1	[7.97, 8.15]	[-0.49, 0.50]	[-2.59, 2.59]	0.22
Northern Vertical about L_2	[7.97, 8.15]	[-5.87, 5.81]	[-5.80, 5.80]	5.84
Axial about L_1	[7.97, 8.15]	[-3.26, 2.68]	[-2.38, 2.38]	1.22

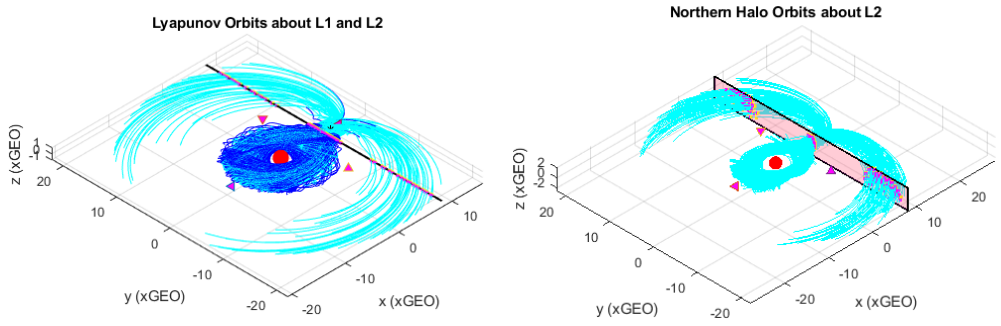

(a) Lyapunov Manifolds about L_1 and L_2 (b) Northern Halo Manifolds about L_2

Fig. 9: Poincaré Surface Maps and Invariant Manifolds

Table 5 shows a composite PSM generated that captures all of the modeled manifold crossings. This was achieved simply by using the minimum and maximum bounds in the three cardinal directions (X, Y, Z) from Table 4.

Table 5: Definition of the PSMs for the Invariant Manifolds

PSM #	X-Bounds (xGEO)	Y-Bounds (xGEO)	Z-Bounds (xGEO)	Volume Increase over 1xGEO
1	[7.97, 8.15]	[-20.44, 20.45]	[-15.31, 16.12]	55.42

2.1.3 Periodic Orbits

Once the RSO has completed its transit, it will enter a periodic orbit for its final destination. The orbit may be about L_1, the Moon, or L_2. The NASA JPL 3-body website [10] has a variety of periodic orbit starting conditions which can be propagated. A list of those investigated are defined in Table 6.

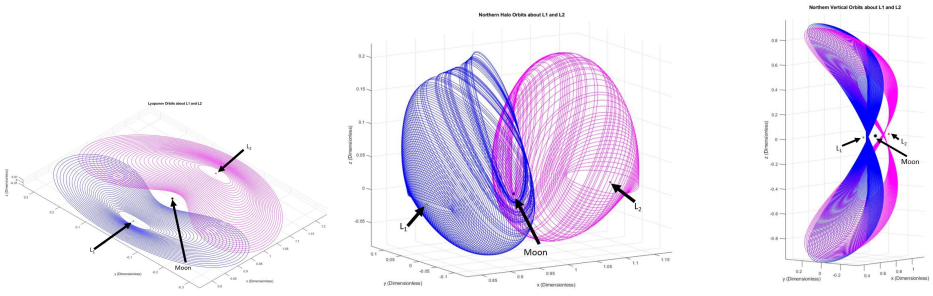

(a) Lyapunov family of orbits (b) Halo family of orbits (c) Vertical family of orbits

Fig. 10: Examples of various periodic orbits about L_1 and L_2 that are used in this research [4]

Table 6: CR3BP Orbit Families from JPL database [10] investigated

Family Name	Orbiting About	Period (days)
Lyapunov	L_1 & L_2	11 - 37
Northern Halo	L_1 & L_2	3 - 16
Southern Halo	L_1	8 - 14
Northern Vertical	L_1 & L_2	17 - 28
Axial	L_1	17 - 18
Southern Dragon Fly	L_1	24 - 32
Distant Retrograde Orbits (DROs)	Moon	0.15 - 28

Consider the Southern Halo Family shown in left figure of Figure 11. Two rectangular PSMs are placed between the Earth and Moon. The pink plane is located roughly half-way between the Earth and Moon and the yellow plane is at the X bounds location defined in Table 2 in Section 2.1.1. The pink plane only captures the largest of the orbits in the family, whereas moving the PSM closer to L_1 captures more of the family. Each orbit crosses the plane twice on its orbital path in a symmetric pairing with one "outgoing" crossing followed by a "return" crossing.

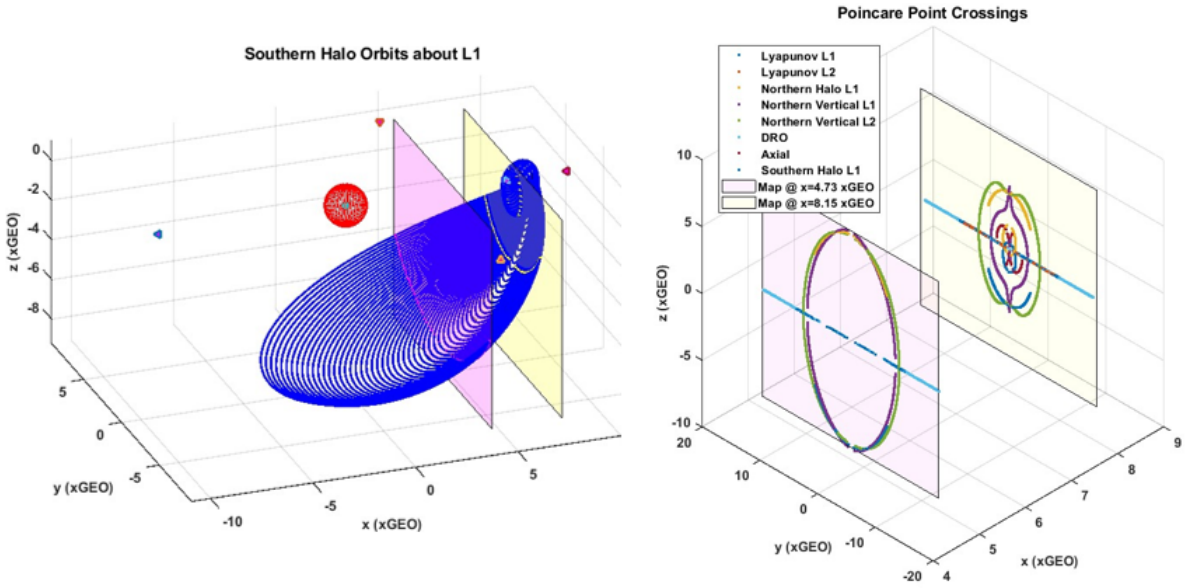

Fig. 11: Left figure shows two PSMs, the Southern Halo Family about L_1, and their intersection. The right figure shows PSMs and a point cloud of intersection for some of the families defined in Table 6.

The figure on the right in Figure 11 shows the same two planes, but includes all of the orbital families defined in Table 6 with all of the family crossings of the two PSMs. The PSM closer to L_1 (yellow plane at 8.15xGEO radii) captures more of the crossings and distinct familial patterns start to emerge which can be used for identification. The spread of the periodic orbit crossings in the yellow PSM reduces in size along the z-axis when compared to the red PSM placed at 4.73xGEO radii. Notice that not all of the families cross the initial PSM. Some of the periodic families such as the Northern Halo about L_2 and Southern Dragonfly require a second PSM. The PSM locations and volume comparison to 1xGEO are found in Table 7.

Table 7: Definition of the PSMs for the Periodic Orbits

PSM #	X-Bounds (xGEO)	Y-Bounds (xGEO)	Z-Bounds (xGEO)	Volume Increase over 1xGEO
1	[7.97, 8.15]	[-14.49, 14.78]	[-4.65, 4.74]	11.85
2	[9.82, 10.0]	[-13.76, 14.04]	[-2.23, 1.88]	4.93

2.1.4 Bounding by Energy

An interesting method involves using the physics of the manifolds and the periodic orbits defined in Table 6. There is an energy field called the Zero-Velocity Surface (ZVS) which controls the size and shape of the manifolds and periodic orbits. Any RSO that interacts with the ZVS will "bounce-off" the surface in a different direction. More accurately, the gravity well at the location of intersection will reduce the velocity of the RSO in the direction of the ZVS such that at the time of intersection, the velocity will be zero, and the acceleration will be in a different direction. The shape and volume of the ZVS is controlled by the Jacobi Constant (Eq. 1 and Eq. 2), which is defined by the starting parameters of the periodic orbits.

$$C = 2U^* - \bar{v}^2 \qquad (1)$$

$$C = (x^2 + y^2) + \frac{2(1-\mu)}{d} + \frac{2\mu}{r} - n^2(\dot{x}^2 + \dot{y}^2 + \dot{z}^2) \qquad (2)$$

(x, y, z) is the position of the RSO, $(\dot{x}, \dot{y}, \dot{z})$ is the velocity or the RSO, and μ is the mass ratio of the Earth-Moon system. The values d and r are the vector magnitude distance from the Earth to the RSO, and Moon to RSO respectively.

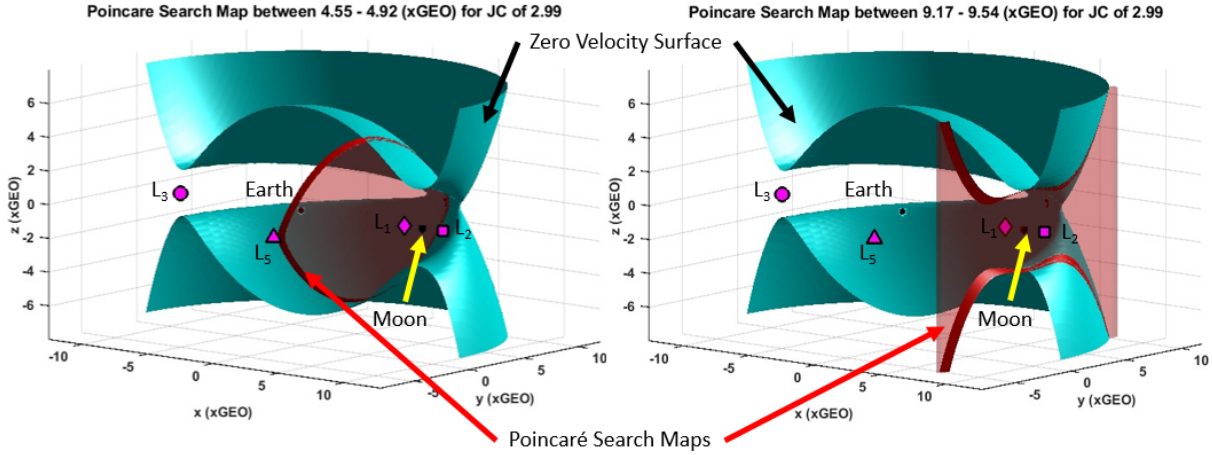

Fig. 12: PSMs (red) bounded by a ZVS. The location of the PSM on the left is half-way between the Earth and Moon. The PSM on the right encompasses the Moon.

For visual purposes the ZVS in Figure 12 are cropped in half to show the inner extent of the volume. The Jacobi Constant chosen for this example would be used for higher energy transfers and orbits. The PSMs mold to the figure of the ZVS and its shape is very dependent on the location and the Jacobi Constant. An advantage of this approach is the periodic orbits and manifolds are constrained by their Jacobi Constant value, bounding the mission cases. As the Jacobi Constant gets larger, the ZVS volume shrinks which also reduces the size and volume of the PSM. Similar to the previous sections, as the PSM gets closer to L_1 it shrinks.

3. RESULTS

To demonstrate the value of this volume reduction process, various aspects of its effectiveness were analyzed. The assessment focused on how an optimized architecture handled direct transfers, low-energy manifolds, and periodic orbits intersecting with the PSMs.

The analysis examined the impact of an architecture on both observability and capacity. For a detailed analysis and motivation of observability vs. capacity, see [11]. In short, observability is defined as the field of regard subject to external constraints (such as solar phase angle and exclusion angles) that a sensor is capable of viewing at a given time. In contrast, capacity is defined as the actual amount a sensor can observe given detailed constraints such as the field of view, sensor constraints, and slew and settle times. When designing an architecture, it was crucial to consider the effects which reduce sensitivity.

First, the performance of the technique was investigated during 3-5 day Earth-Moon transfers that crossed the PSMs, assessing its effectiveness. Next, the technique was applied to manifolds, providing insights into its utility within more complex geometrical contexts. The evaluation then addressed how well the technique managed periodic orbit crossings through the PSMs, examining its effectiveness in different crossing situations. Finally, the combination of all three scenarios was analyzed simultaneously to understand how the technique performed when addressing multiple types of crossings at once.

An optimized architecture for the PSMs defined in Tables 2, 4, and 7 was chosen based on capacity using an in-house tool described in [12]. For this analysis, a single optimized architecture was selected and its performance was compared on the direct transfer (Hohmann) crossings through the PSMs, the manifold crossings through the PSMs, the periodic orbit crossings through the PSMs, and finally all combined volumes. The architecture chosen is shown in Table 8 and Figure 13. The numbers labeled in Figure 13 correspond the type of orbit in Table 8.

SV #	Orbit Family
1	Eastern Low Prograde
2	Western Low Prograde
3	Southern L2 Halo
4	L5 Vertical
5	L5 Vertical
6	Northern Butterfly
7	Northern Butterfly
8	Distant Prograde
9	L5 Long Period

Table 8: Selected Optimized Architecture

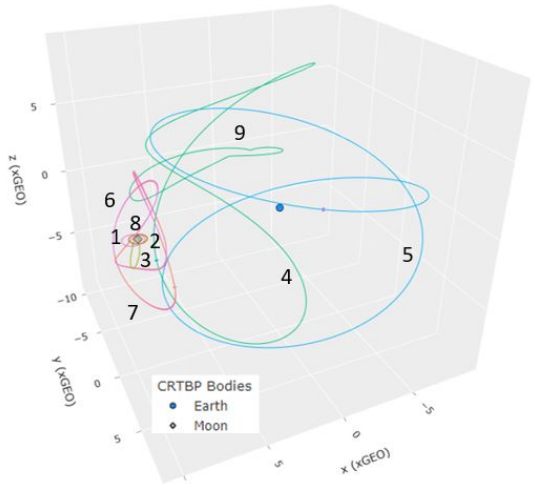

Fig. 13: Selected Optimized Architecture Orbits

For each scenario, the architecture's performance was assessed over a complete synodic period. This involved using one-hour samples distributed evenly throughout the period and calculating their average. This approach aimed to evaluate how consistently the architecture could observe each volume of points. The one-hour interval was chosen because it represented the shortest traversal time the trajectories through the defined PSMs, thereby maximizing the likelihood of detecting the full range of possible trajectories. An example of this is shown in Figure 14. The histogram plot displays the time between the periodic orbit entering and exiting the PSM. The x-axis is the number of hours the trajectory is within the PSM, and the y-axis number of orbits with a specific traversal duration. Out of 48,190 crossings, 24 orbits spent less than an hour within the PSM boundaries.

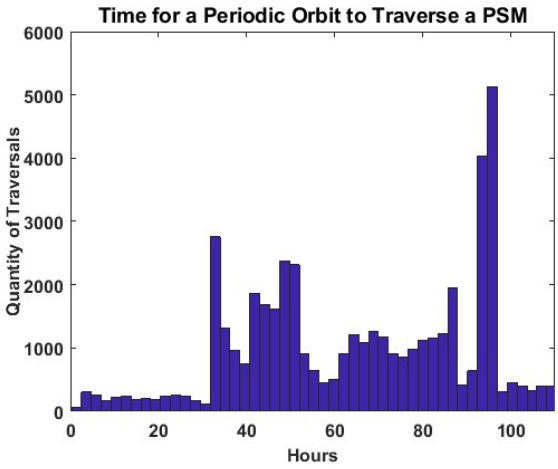

Fig. 14: Periodic orbital traversal times through the PSM

3.1 Individual Volume Analysis

First, the performance of the architecture defined in Table 8 was analyzed across various scenarios, focusing on the different PSM volumes described in Section 2.1. Namely, the direct transfer (Hohmann-like) trajectories, manifolds, and periodic orbits crossing through the PSMs relevant to the mission.

Figures 15 - 17 illustrate the results of the analysis for each volume. Data was sampled over a full synodic period, the 'best' and 'worst' cases across the synodic period are shown for each PSM volume. In these figures, the red dots indicate the regions within the volumes that were not observed. The non-red dots represent the observed regions, with the frequency of observation depicted by the color gradient corresponding to the color bar in each figure. This visual representation distinguishes between observed and non-observed areas, while also conveying the frequency of observation across the volumes.

The first analysis considered the performance on the volume defined by the Hohmann transfers passing through the PSMs, as described in Section 2.1.1. The results are depicted in Figure 15, which show the best and worst viewing times over the synodic period. On January 8, 2025, the architecture achieved a maximum capacity of 100.00%. Even at the worst viewing time, January 15, 2025, a substantial capacity of 99.39% was maintained, demonstrating the architecture's ability to monitor a significant portion of the trajectories of interest, even under less favorable conditions.

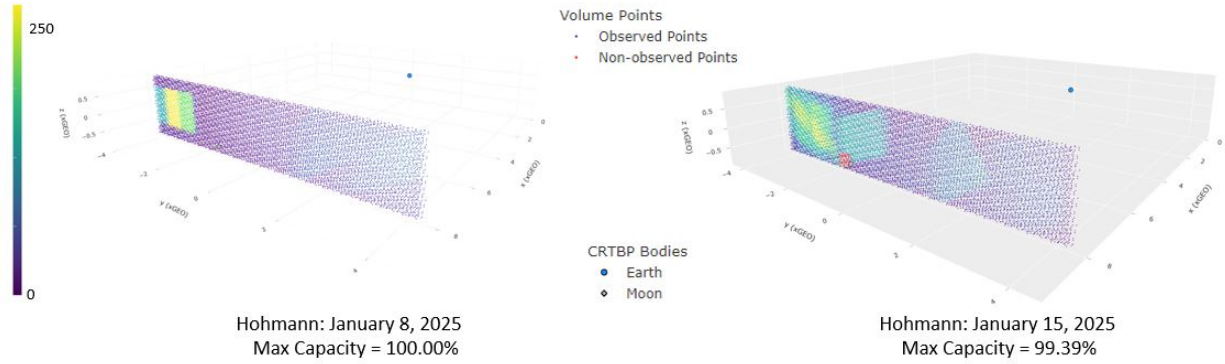

Fig. 15: Capacity for Hohmann Transfers crossing through the PSMs

The second scenario evaluated the architecture's performance on the low-energy manifold crossings, as detailed in Section 2.1.2. The best performance for this volume occurred on January 15, 2025, with a maximum capacity of 95.59%, while the worst performance on January 1, 2025, resulted in a capacity of 84.77%. Figure 16 illustrates these results, indicating that the architecture consistently captured the majority of relevant trajectories, even at its lowest performance.

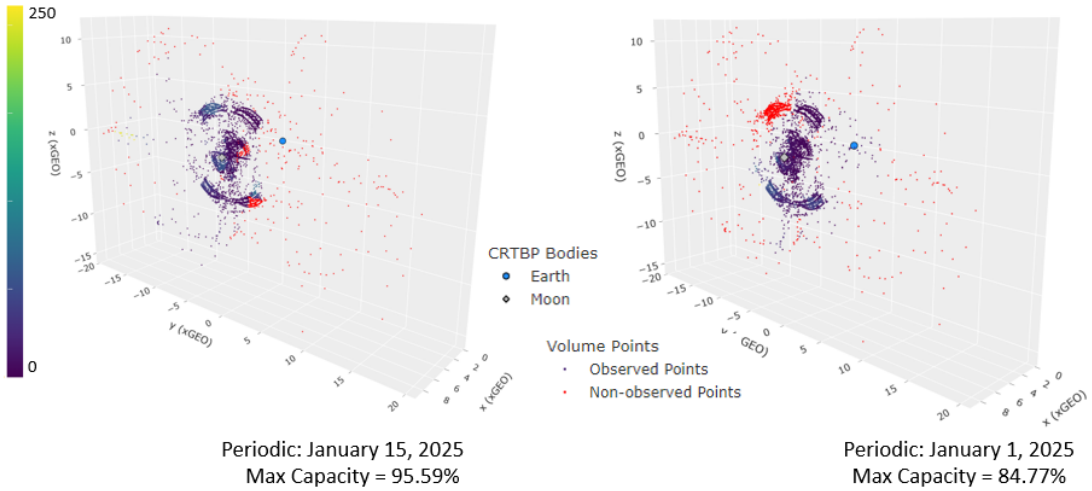

Fig. 16: Capacity for manifolds crossing through the PSMs

In the analysis of the periodic orbit PSMs crossings, outlined in Section 2.1.3, the architecture once again demonstrated

strong performance. The maximum capacity reached 99.59% on January 15, 2025, and even at the worst performance on January 1, 2025, the architecture achieved an 84.38% capacity. Figure 17 presents these findings, confirming that the architecture maintained a high level of effectiveness throughout the synodic period. The localized red points at the bottom right on the left figure, and top left for the figure on the right are a result of poor solar phase angles impacting illumination in those regions.

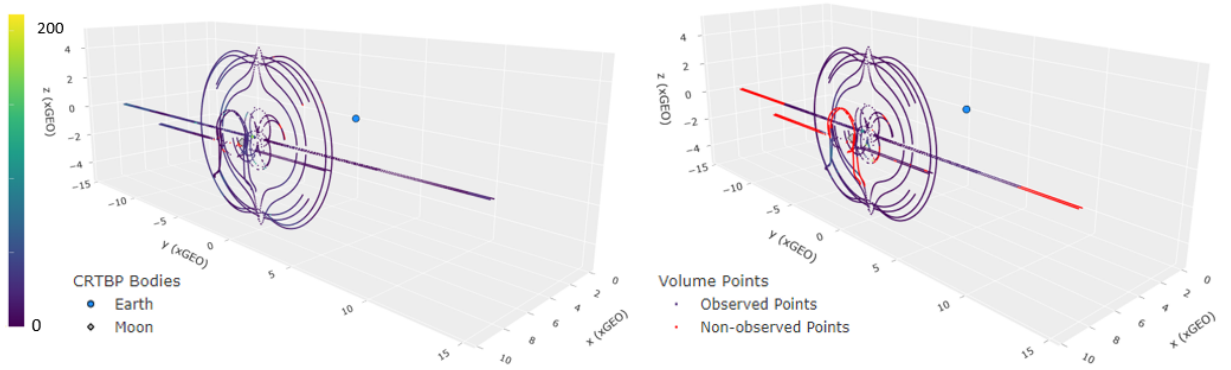

Periodic: January 15, 2025
Max Capacity = 99.59%

Periodic: January 1, 2025
Max Capacity = 84.38%

Fig. 17: Capacity for periodic orbits crossing through the PSMs

This analysis evaluated the performance of the architecture across various mission-relevant PSM volumes, including direct transfer trajectories, low-energy manifolds, and periodic orbits intersecting with key mission points. The figures illustrate the architecture's ability to consistently observe a significant portion of the trajectories, even under less favorable conditions, throughout the synodic period. The results demonstrates that the architecture maintained strong observation capabilities across all volumes, effectively capturing the majority of relevant trajectories, which highlights the robustness and effectiveness of using PSMs to reduce the search volume while maximizing detection coverage in the cislunar region.

3.2 All Crossings

After analyzing the performance of the architecture on each individual volume, the analysis was extended to evaluate its performance across all PSM volumes simultaneously. This approach demonstrated the architecture's ability to observe nearly all possible space vehicles of interest traversing the cislunar space while significantly reducing the observed volume.

Figure 18 reflects this analysis, similar to the previous section, where red dots indicate unobserved regions and non-red dots represent observed regions. The color bar illustrates the frequency with which different parts of the volume were observed. This analysis revealed that on January 8, 2025, the combined volume reached a maximum capacity of 96.07%, while still maintaining substantial capacity of 84.72% even at the worst viewing time on January 1, 2025. These findings underscore the architecture's robust and reliable performance across various mission scenarios.

Figure 19 provides a summary of the architecture's performance for the volume consisting of all the crossings, demonstrating its capability to monitor 90% of all crossings within just 0.35 hours using a 9-space vehicle (SV) configuration during its best viewing conditions. Even during the least favorable conditions on January 1, 2025, over 80% of the crossings were still observed within 0.8 hours. A summary of the architecture's performance across all volumes can be seen in Table 9.

These results highlight the robustness and reliability of using PSMs to minimize the searchable volume, proving its value in ensuring comprehensive coverage across varied mission scenarios while minimizing mission costs. The results shown above indicate that using a small 9-SV architecture, nearly all of the cislunar space of interest was close to persistently detectable. This performance is particularly impressive when compared to the estimated 70-SV architecture designed for 10xGEO observations [2]. This technique is a powerful method for mission planning and execution in cislunar space. Given the high cost of space-based sensors, the volume reduction process offers a significant advantage by potentially reducing the number of required spacecraft by an order of magnitude while still capturing a substantial portion of the trajectories within the volume of interest.

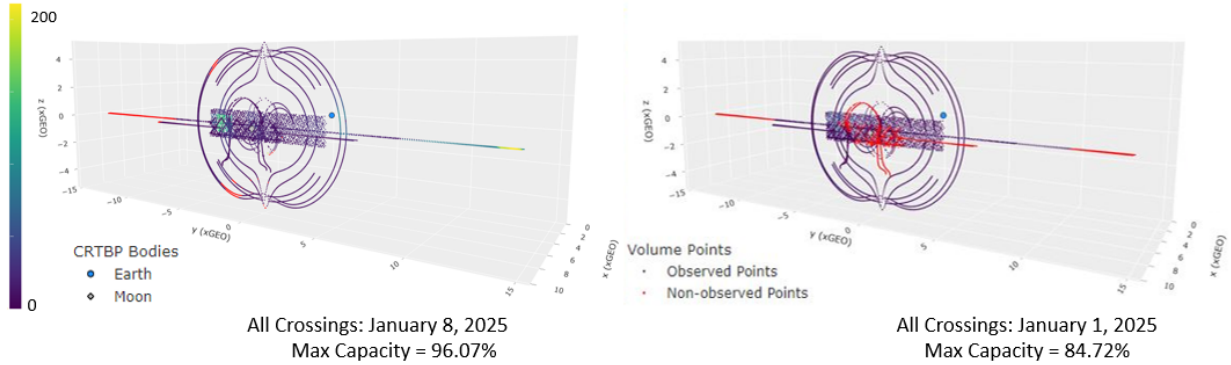

Fig. 18: Capacity for all crossing through the PSMs

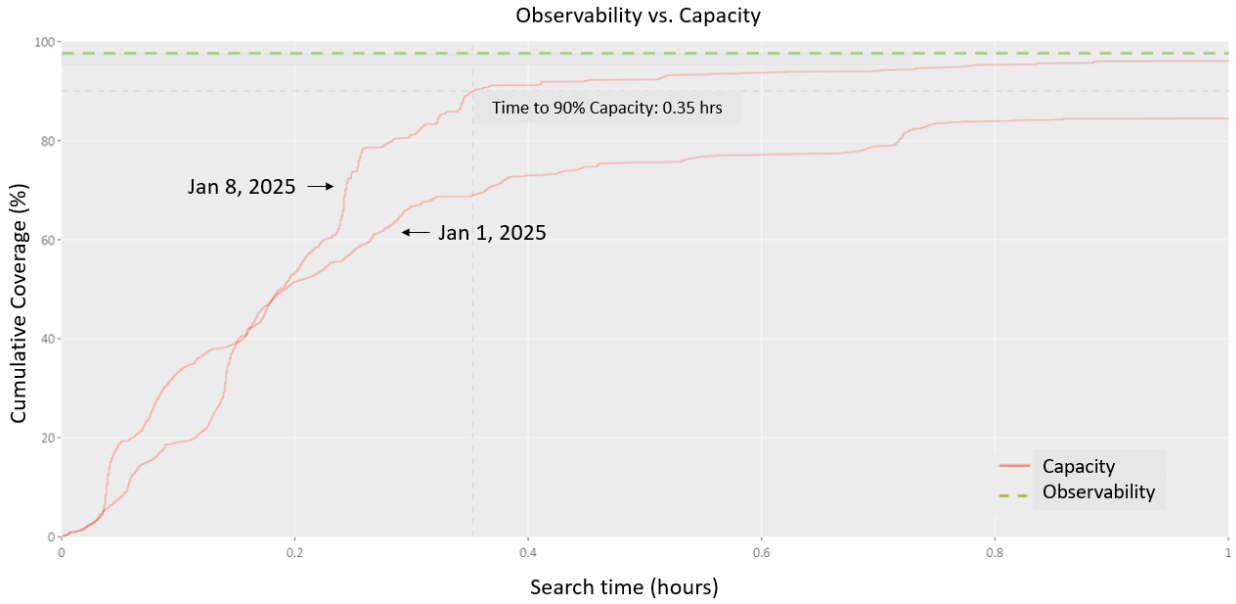

Fig. 19: Observability vs. Capacity for All Crossings

	Manifold		Periodic		Hohmann		All Crossings	
Date	**Observability %**	**Capacity %**	**Observability %**	**Capacity %**	**Observability %**	**Capacity %**	**Observability %**	**Capacity %**
Jan 1	98.07	84.77	93.00	84.38	99.95	99.94	96.18	84.72
Jan 8	98.61	95.14	95.33	92.35	100.00	100.00	97.44	96.07
Jan 15	98.35	95.59	99.93	99.59	99.39	99.39	99.72	93.61
Jan 22	96.97	90.61	95.05	93.01	100.00	100.00	97.31	93.43
Average	**98.00**	**91.53**	**95.83**	**92.33**	**99.84**	**99.83**	**97.66**	**91.96**

Table 9: Performance of Different Architectures for January 2025 Sampled Data

4. CONCLUSIONS

In conclusion, the integration of Poincaré Search Maps (PSMs) into Cislunar Space Domain Awareness (SDA) marks a transformative advancement in the optimization of object detection and tracking within the vast cislunar environment. The unique approach of strategically placing virtual surfaces in high-traffic areas significantly reduces the search volume, thereby enhancing detection capabilities and improving the overall efficiency of space missions. This reduction in search space is particularly critical given the increasing complexity and scale of operations in cislunar space, where

the vast distances and dynamic trajectories present significant challenges for traditional monitoring methods.

The four scenarios examined in this study—ranging from periodic orbit crossings to the application of complex manifolds—underscore the versatility and robustness of PSMs across various operational contexts. Each scenario highlights how PSMs can be tailored to specific mission needs, providing a flexible framework that can adapt to the evolving landscape of cislunar space. The ability of PSMs to efficiently handle both routine and complex trajectories ensures that SDA efforts remain effective even as space traffic increases and operational demands grow.

As space activity in the cislunar region continues to intensify, driven by both governmental and commercial interests, the need for robust and adaptable space surveillance architectures becomes more urgent. The insights gained from this study offer valuable guidance for the development of future SDA systems, emphasizing the importance of integrating advanced tools like PSMs into the broader surveillance strategy. By enhancing proactive space monitoring, PSMs not only contribute to mission success but also play a crucial role in maintaining the safety and security of cislunar operations.

In summary, this study highlights the significant potential of PSMs to revolutionize cislunar SDA by providing a powerful tool for optimizing search and detection processes. As space exploration and utilization expand, the continued development and refinement of PSM-based approaches will be essential in ensuring the sustainable and secure growth of activities in the cislunar domain.

REFERENCES

[1] Johnson, K., "Fly me to the moon: Worldwide cislunar and lunar missions," in [*Washington, D.C.: Center for Strategic and International Studies*], CSIS AEROSPACE SECURITY PROJECT (2022).

[2] Wysack, J. and Ferrant, K., "Contrasting Architectures for Cislunar SDA and STM," in [*Proceedings of the Advanced Maui Optical and Space Surveillance (AMOS) Technologies Conference*], Ryan, S., ed., 207 (Sept. 2023).

[3] Holzinger, M., Chow, C. C., and Garretson, P., "A primer on cislunar space," *AFRL* **1271** (2021).

[4] Wright, R., Tafur, L., Owens Fahrner, N., and Wysack, J., "Monitoring and Tracking Accessible Invariant Manifolds in The Cislunar Regime," in [*Proceedings of the Advanced Maui Optical and Space Surveillance (AMOS) Technologies Conference*], Ryan, S., ed., 204 (Sept. 2023).

[5] Bloom, A., Wysack, J., J., G., and A., L., "Space and Ground-Based SDA Sensor Performance Comparisons," in [*Proceedings of the Advanced Maui Optical and Space Surveillance (AMOS) Technologies Conference*], (Sept. 2022).

[6] Hohmann, W., [*The Attainability of Heavenly Bodies*], NASA, Washington (1960).

[7] Biesbroek, R. and Janin, G., "Ways to the moon?," *ESA bulletin. Bulletin ASE. European Space Agency* **103**, 92–99 (08 2000).

[8] Belbruno, E. A. and Miller, J. K., "Sun-perturbed Earth-to-moon transfers with ballistic capture," *Journal of Guidance Control Dynamics* **16**, 770–775 (Aug. 1993).

[9] NASA, "Horizon systems," *https://ssd.jpl.nasa.gov/horizons/app.html* (2024).

[10] NASA, "Three body periodic orbits," *https://ssd.jpl.nasa.gov/tools/periodic_orbits.html/intro* (2024).

[11] Owens Fahrner, N., Correa, J., and Wysack, J., "Capacity-based cislunar space domain awareness architecture optimization," in [*Advanced Maui Optical and Space Surveillance Technologies Conference*], (2022).

[12] Kim, J. and Owens-Fahrner, N., "A comprehensive approach to optimized cislunar architecture design utilizing capacity," in [*Advanced Maui Optical and Space Surveillance Technologies Conference*], (2024).